Journal of Directed Energy, **4**, Winter 2010, 189–204

Fluence and Wavelength Dependence of a Painted Surface Absorptance during Short-Pulse Laser Illumination

Michael E. Thomas,* Daniel V. Hahn, and Kevin C. Baldwin

Applied Physics Laboratory, Johns Hopkins University, Laurel, Maryland 20723

and

Caroline McEnnis and James B. Spicer

Department of Material Science and Engineering, Johns Hopkins University, Baltimore, Maryland 21218

The absorptance of an opaque surface is completely characterized by the surface bidirectional reflectance distribution function (BRDF). In particular for this study, a laser-ablated, painted aluminum substrate is characterized in terms of its BRDF. The sample is exposed to a raster-scanned high-intensity Ti:sapphire laser operating up to a 1-kHz pulse repetition frequency with pulse duration of around 150 fs and pulse energies up to 650 μJ at a wavelength of 800 nm. The ablated surface is then characterized in terms of a measured BRDF at 633, 1,064, and 3,390 nm. In this way the specular and diffuse nature of the paint can be determined. A novel physics-based semiempirical model is used to represent the data as a function of laser fluence and wavelength. How the model can handle such time (fluence)-dependent phenomena is discussed. Such a capability is essential in representing the light–matter interaction between the laser beam and target.

KEYWORDS: Absorptance, BRDF, Diffuse reflectance, Fluence, High-energy lasers, Specular reflectance

Nomenclature

A	area, m^2
a	albedo
$\mathrm{BRDF}(\Omega_i, \Omega_r)$	bidirectional reflectance distribution function, 1/sr
d	slab thickness, m
E_p	pulse energy, J
E_ν	photon energy, J
E_0	damage threshold energy, J
F	fluence, J/m^2
F_{th}	fluence threshold, J/m^2
f	photon frequency, Hz
$H(\theta, \theta_i)$	top-hat function

Received December 2009; revision received October 10, 2010.

*Corresponding author; e-mail: Mike.Thomas@jhuapl.edu.

h	Planck's constant
I	intensity, W/m^2
k	index of absorption
M_ν	number of photons
m	exponent (in parameterized scatter phase function model)
N	normalization factor
n	refractive index
$\bar{n}$	complex index of refraction
PRF	pulse repetition frequency, Hz
$P(\Omega_i, \Omega_r)$	scatter phase function, 1/sr
Q_{ext}	extinction efficiency
R	Fresnel reflection coefficient
r	distance from sample to detector, m
r_d	detector radius, m
r_p	particle radius, m
t_{scan}	ablation scan time, s
α	half-angle, rad
α_{abs}	absorptance
α_{sca}	scatterance
β_{abs}	absorption coefficient, $1/m$
β_{sca}	scatter coefficient, $1/m$
γ	rate factor
η_p	particle size distribution function
θ	polar angle, rad
λ	wavelength, m
ρ	reflectance
τ	transmittance
Φ	flux, W
ϕ	azimuthal angle, rad
Ω	solid angle, sr
ω	angular frequency, rad/s

1. Introduction

Material damage or processing by high-energy lasers has been studied for a long time.[5,9] Topics include laser damage of optical components, laser machining (cutting, welding, etc.), surface ablation, and so on. Damage phenomena can be classified into two major groups. Short-duration pulses of less than 20 ps cause damage by electron excitation via multiphoton absorption; at such timescales, electrons have insufficient time to couple to the lattice during the laser pulse.[9] This results in energy transfer to the translational motion of molecules (on a timescale faster than the mechanical relaxation of the system), inducing *localized* thermal and pressure increases. When the pressure gradient in the direction normal to the surface exceeds the mechanical strength of the material, molecules are ejected or ablated from the surface.[5]

Generally, long-duration pulses with widths greater than 20 ps cause thermal damage by target melting and spalling. Specifically, incident laser radiation heats conduction-band electrons and transfers energy to the lattice. This *bulk* heating can melt, boil, or fracture the material.[9]

Of particular interest in this study is high-energy laser coupling into a painted target by a subpicosecond-class laser as a function of the laser fluence (also exposure time) and illumination wavelength. This is accessed by determining the surface absorptance by direct measurement of the surface reflectance (the sample is opaque). A bidirectional reflectance distribution function (BRDF) model is used to represent and extend the data; the BRDF also provides the classification of the reflected rays as near specular or diffuse. Furthermore, the power spectral density (PSD) function can be computed from the BRDF and used to calculate the surface root-mean-square roughness.[4]

Over the past several years a variety of BRDF measurements have been collected at the Applied Physics Laboratory of Johns Hopkins University. The samples include coated (e.g., painted) surfaces, metals, transmissive windows, and cylindrical fibers (e.g., string). A set of semiempirical functions have been successfully applied to represent these data. These bidirectional functions are often non-Gaussian in nature,[7] which differs from traditional Legendre-type functions.[1,3] A power law fall off is typically observed in the experimental results, especially for diffuse surfaces. The functions presented in this paper are similar to the Lorentz class of functions generally used in spectral line shape theory.

2. Experiment

A Rustoleum® 1904 gloss white paint sample is exposed to an amplified mode-locked Ti:sapphire laser operating at 800 nm with pulse duration of approximately 150 fs, pulse energy of 650 μJ, and pulse repetition frequency (PRF) between 12 and 1,000 Hz. The laser is focused to a spot size diameter of 250 μm on the sample and scanned to create an ablated area 7.15 × 7.15 mm^2. Computer-controlled motion actuators/stages were used to ensure the uniformity of the ablation area. Scan lines across the area were made at a constant velocity and duration of 3.5 s each; adjacent scan lines were separated by either 0.20- or 0.15-mm raster steps to achieve laser spot overlap to create a degree of ablation uniformity. The illuminating fluence F is computed using the following definition:

$$F = \frac{t_{\text{scan}} E_p \text{PRF}}{A_{\text{ab}}}, \tag{1}$$

where t_{scan} is the time it takes to scan the ablated area A_{ab} with pulse energy E_p. For the operating parameters for this particular laser, a PRF of 12 Hz essentially represents an illumination by one pulse for any given point within the ablated area. In this manner, the surface evolution can be characterized in terms of the illuminating fluence or the number of effective pulses that illuminate the target area. The fluence is varied by varying the laser PRF, and thus a series of ablated areas is created. The absorptance of these areas is characterized by measuring the BRDF.

A description of a scatterometer/reflectometer (ignoring polarization effects and assuming no azimuthal dependence) used to measure the BRDF over the back hemisphere is given below. In this case only measurements in the plane of incidence are required. Such measurements are used to represent a wide variety of materials.

A direct measurement of the incremental backscattered flux $\Delta\Phi(\theta_r, \theta_i)$ per incremental steradian $\Delta\Omega$ is proportional to the phase function $P(\theta_r, \theta_i)$ (Ref. 6):

$$\frac{\Delta\Phi(\theta_r, \theta_i)}{\Phi_i \, \Delta\Omega} = \text{BRDF}(\theta_r, \theta_i) = \rho_{\text{hem}}(\theta_i) P(\theta_r, \theta_i), \tag{2}$$

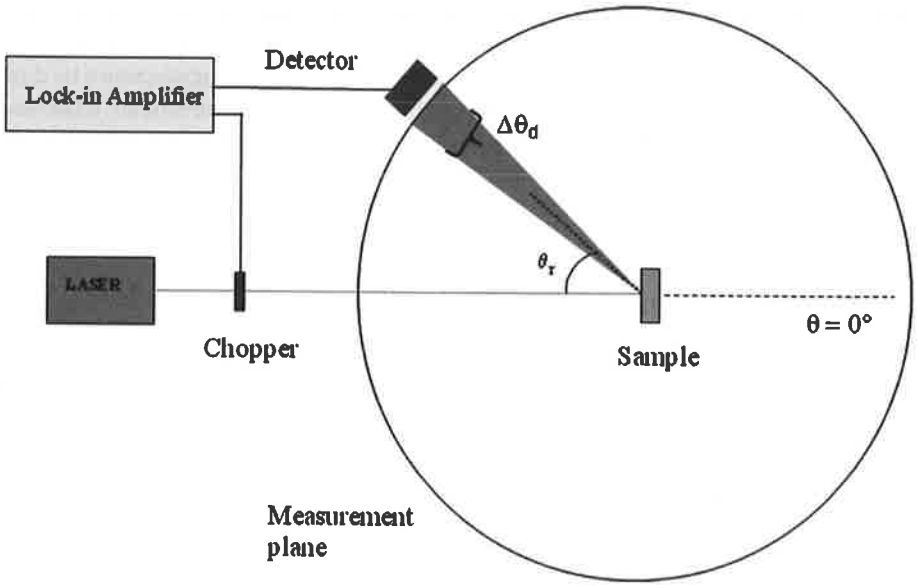

Fig. 1. Experimental setup of a bidirectional scattering measurement to obtain the in-plane BRDF.

where Φ_i is the incident flux, BRDF(θ_s, θ_i) is the bidirectional reflectance distribution function, and $\rho_{\text{hem}}(\theta_i)$ is the total integrated reflectance (TIR). In practice the measured fluxes are detector voltages. Since there is no dependence on sample rotation about ϕ_r, only measurements in the θ_r direction are required. The incremental angular step size of θ_r for the experiment should be less than $\frac{1}{2}\Delta\Omega$.

The incremental solid angle $\Delta\Omega$ can be determined from the experimental geometry as illustrated in Fig. 1. It is given by the following formula:

$$\Delta\Omega = 2\pi(1 - \cos\Delta\theta_d), \tag{3}$$

where $\Delta\theta_d$ is the angle subtended by the detector. For $r \gg r_d$ (the detector radius), $\Delta\theta_d$ is small and the following approximation can be made:

$$\Delta\Omega = 2\pi\left\{1 - \frac{r}{r\left[1 + \left(\frac{r_d}{r}\right)^2\right]^{1/2}}\right\} = \frac{\pi {r_d}^2}{r^2}. \tag{4}$$

The detector area A_d is πr_d^2, and the incremental solid angle viewed by the detector becomes

$$\Delta\Omega \to \frac{A_d}{r^2}. \tag{5}$$

Using this result in Eq. (1) completes the information needed to experimentally determine the BRDF of a sample.

The apparatus used to measure BRDFs is illustrated in Fig. 1. The source laser beam is chopped and expanded and focused (using reflective optics) onto a detector mounted

on a rail, which is in turn mounted on a rotational stage. The sample is mounted at the center of rotation of the detector-rail system such that the plane of incidence is parallel with the tabletop. This allows for measurement of the full BRDF, including the specular reflection. Again, we have made the assumption that scatter is symmetric with respect to the surface normal (i.e., that the scattered intensity has no dependence on the azimuthal angle). The detector is rotated around the sample and the detector output recorded by a lock-in amplifier whose reference signal is derived from the chopper. Measurements in the visible use a silicon detector with a square active area of 0.13 cm^2; measurements in the midinfrared (IR) use an InSb detector with a circular active area of 0.0314 cm^2. The typical distance from the sample to the detector is 30 cm.

3. BRDF Model

All the BRDF experimental data are fitted to physically based models for three primary reasons. The first is to compensate for limitations of the measurement. For example, the detector blocks the incident beam at some point in the BRDF depending on the angle of incidence. This leads to a dropout in the reflected signal. This is a significant effect for near-normal illumination and leads to an underestimation of the TIR (also called the directional hemispherical reflectance). Second, for oblique illumination angles the sample alignment is critical and mounting posts can partially block the reflected beam, leading to signal distortion. Finally, as the sample plate is rotated from normal to oblique angles, the illuminating spot grows in the plane of incidence but remains fixed in the direction orthogonal to the plane of incidence. Thus, the computation of the TIR must take the resulting reflected beam shape into account because it will not be the same in all directions of ϕ for all θ_i.

Another reason for model fitting is to check the observations against our theoretical understanding of reflection phenomena. A fundamental quantity modeling surface reflectance is the complex index of refraction $\bar{n}$, given by

$$\bar{n} = n - jk, \tag{6}$$

where n is the index of refraction and k is the index of absorption. Although all samples absorb at some level, it is assumed that $k \ll n$. Thus, the surface reflectance is typically dominated by the real part of the complex index of refraction only. In the BRDF measurement results, two distinct phenomena are observed. A percentage of the BRDF is completely diffuse (or Lambertian) and independent of the angle of incidence, and the remaining portion of the BRDF follows an angle-averaged, power reflection coefficient Fresnel equation and depends on the angle of incidence.

The following equation defines a bidirectional reflection function[6]:

$$\frac{d\Phi}{d\Omega_r} = \mathrm{BRDF}(\Omega_i, \Omega_r, \omega)\Phi_i. \tag{7}$$

In this equation, the BRDF(Ω_i, Ω_r, ω) is called the bidirectional reflectance distribution function, Ω_i is the illumination beam solid angle, Ω_r is the reflected beam solid angle, and ω is the angular frequency. In these definitions of BRDF, Ω_r covers the backward hemisphere. BRDF measurements are typically for nontransmitting samples (e.g., mirrors, painted surfaces). These concepts are illustrated in Fig. 2. Also, in this development the polarization state of the scattered optical fields has not been addressed. It is assumed that the observer is not concerned with polarization.

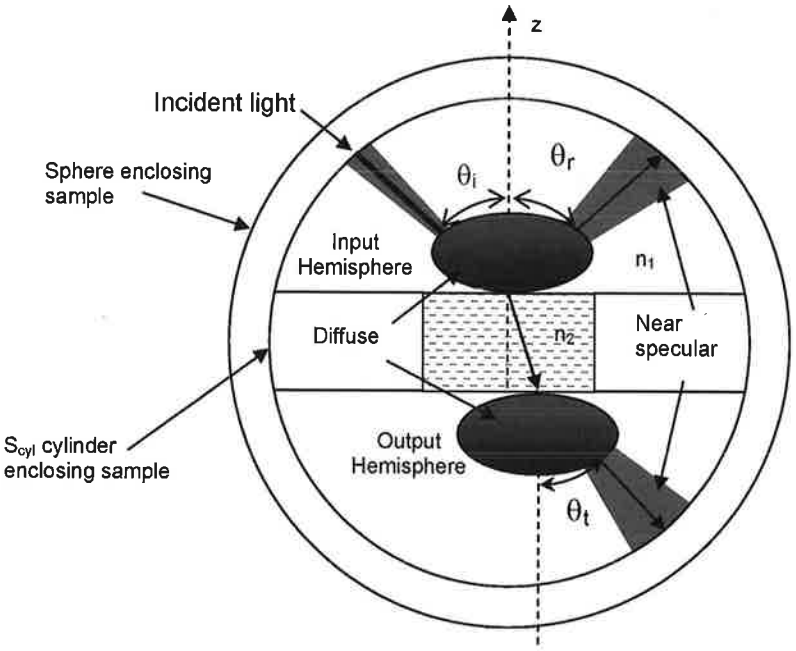

Fig. 2. Geometrical concepts of specular and diffuse components of transmitted and reflected light from an illuminated dielectric slab.

The integral of the BRDF over all back reflected solid angles Ω_r is the TIR,

$$\rho_{\text{hem}}(\Omega_s) = \int_{\text{hemisphere}} d\Omega_r \text{BRDF}(\Omega_r, \Omega_s). \tag{8}$$

Based on this definition, the BRDF is broken down as a product of two factors, the total integrated quantity and a normalized solid angle-dependent function called the phase function $P_{r,s}(\Omega_i, \Omega_{r,s})$ for reflection and scatter, respectively. The BRDF is now written as

$$\text{BRDF}(\Omega_i, \Omega_r) = \rho_{\text{hem}}(\Omega_i) P_r(\Omega_i, \Omega_r). \tag{9}$$

Consistent with Eq. (8), all phase functions are normalized according to

$$\int P(\Omega_i, \Omega_r)\, d\Omega_r = 2\pi \int P(\theta_i, \theta_r) \sin(\theta_r, \theta_i)\, d\theta_r = 1, \tag{10}$$

where the limits of integration cover the back hemisphere. Solving this equation determines the normalization factor. In this manner, the phase function has the interpretation of a probability density function. It gives the probability of observing a reflected ray in a particular direction given a specific incidence angle.

The integrated quantities satisfy the total power law:

$$\tau(\Omega_i, \omega) + \rho(\Omega_i, \omega) + \alpha_{\text{sca}}(\Omega_i, \omega) + \alpha_{\text{abs}}(\Omega_i, \omega) = 1, \tag{11}$$

where τ is the transmittance, ρ is the reflectance, α_{abs} is the absorptance, and α_{sca} is the scatterance. This is a statement of the conservation of power flow.

It is useful to separate the BRDF into specular (s), near specular (ns), diffuse (D), and random diffuse (L, Lambertian) components, separately representing the unscattered

beam (specular) and the scattered light, respectively, as given by the following formula for reflectance (back hemisphere):

$$\mathrm{BRDF}(\Omega_i, \Omega_r, \omega) = \rho_S(\Omega_i, \omega)x_S\delta(\Omega_i + \Omega_r) + \rho_{\mathrm{nS}}(\Omega_i, \omega)x_{nS}P_{\mathrm{nS}r}(\Omega_i, \Omega_r, \omega) + \rho_D(\Omega_i, \omega)P_{Dr}(\Omega_i, \Omega_r, \omega) + \rho_L(\omega)x_L P_{Lr}(\Omega_r, \omega). \quad (12)$$

It is assumed that these different types of reflected, transmitted, and scattered light are independent. Specular components (P_S) represent the contributions from the reflected and transmitted rays for a perfectly flat surface. The law of reflection is applied (i.e., $\Omega_\mathrm{r} = -\Omega_\mathrm{i}$) at the specular point in this case. Near-specular components (P_{nS}) represent weak or single-scatter phenomena due primarily to surface roughness such that the coherence of the incident light is maintained. Diffuse components (P_D) represent the effects of surface roughness and bulk scatter that is strongly influenced by multiple scatter and is partially coherent relative to the incident light. The Lambertian components (P_L) represents random rough surface and bulk scatter that is totally incoherent with the incident light. A real surface will have some percentage of the surface that appears flat and some percentage that is rough.

For a uniform surface with randomly oriented surface roughness and bulk inhomogeneities, there will be no dependence in the ϕ direction. Thus, scatter from the sample is invariant under rotation by the angles ϕ_i and ϕ_r, and the phase function is a function of θ_i and θ_r only. This is the case for the samples analyzed in this study.

For example, given a passive medium with no surface roughness (i.e., no surface scatter), no bulk scatter, and a collimated ray bundle with angle θ_i incident on the surface, then the BRDF becomes purely specular; thus

$$\rho(\theta_i, \theta_r, \omega) = \rho_S(\theta_i, \omega)\delta(\theta_i + \theta_r). \quad (13)$$

Again the subscript S denotes specular or flat surface terms where the reflected angle equals the negative of the incident angle and the transmitted angle approximately equals the incident angle (for nearly parallel surfaces; see Fig. 2). Then the generalized total power law reduces to the simple formula[3]

$$\tau_S(\theta_i, \omega) + \rho_S(\theta_i, \omega) + \alpha_{\mathrm{abs}}(\theta_i, \omega) = 1. \quad (14)$$

In principle, these deterministic specular terms are a function of the complex index of refraction for spectrally averaged (that is, the bandwidth of the incident beam washes out interference effects) polarized light incident on a slab of thickness d, as given by (ignoring interference, fluorescence, and diffraction)[3]

$$\tau_S(\theta_i, \omega) = \frac{[1 - R_1(\theta_i, \omega)][1 - R_2(\theta_i, \omega)]\exp[-\beta_{\mathrm{abs}}(\omega)d/\cos\theta_a]}{1 - R_1(\theta_i, \omega)R_2(\theta_i, \omega)\exp[-2\beta_{\mathrm{abs}}(\omega)d/\cos\theta_a]}, \quad (15)$$

$$\rho_{\mathrm{S}}(\theta_i, \omega) = \frac{R_1(\theta_i, \omega) + R_2(\theta_i, \omega)\,[1 - 2R_1(\theta_i, \omega)]\exp[-2\beta_{\mathrm{abs}}(\omega)d/\cos\theta_a]}{1 - R_1(\theta_i, \omega)R_2(\theta_i, \omega)\exp[-2\beta_{\mathrm{abs}}(\omega)d/\cos\theta_a]}, \quad (16)$$

and

$$\alpha_{\mathrm{abs}}(\theta_i, \omega) = \frac{[1 - R(\theta_i, \omega)]\{1 - \exp[-\beta_{\mathrm{abs}}(\omega)d/\cos\theta_a]\}}{1 - R(\theta_i, \omega)\exp[-\beta_{\mathrm{abs}}(\omega)d/\cos\theta_a]}. \quad (17)$$

$R(\theta_i, \omega)$ is the single surface Fresnel power reflection coefficient for polarized or unpolarized light as a function of the angle of incidence θ_i, wave number, and complex index of refraction, and β_{abs} is the absorption coefficient.

In practice, four types of phase functions are used to represent measured data. The instrument (specular) phase function is represented by the Gaussian profile of the illuminating

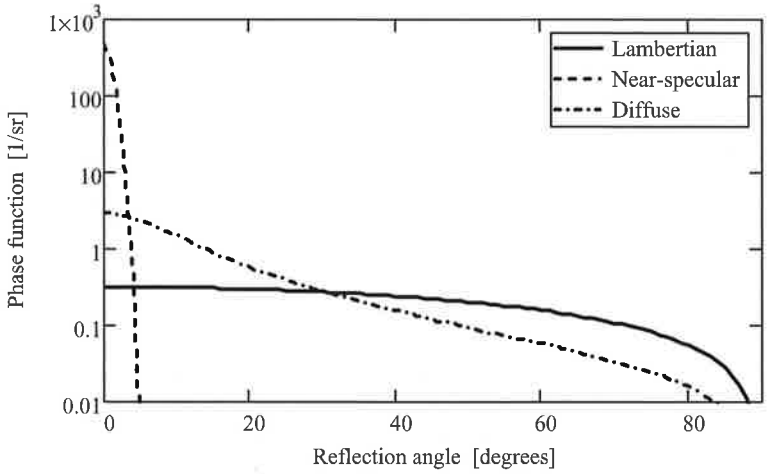

Fig. 3. Comparison of the different phase functions defined in Sec. 3. The near-specular phase function and the diffuse phase function have the same angular width (5 deg). (In all cases the illumination angle is 0 deg.)

laser and is chosen to be

$$P_{\text{instr}}(\theta_r, \theta_i) = P_S(\theta_r, \theta_i) = N_{\text{instr}}(\theta_i, w) \exp\left[-\frac{(\sin\theta_r + \sin\theta_i)^2}{w^2}\right], \tag{18}$$

where θ_r is the reflection angle, θ_i is the incident angle, N_{instr} is a normalization constant, and w is related to the beam width. In addition, surface imperfections may result in the empirical value of $\rho_S(\theta_i, \omega)$ being less than the theoretical value given in Eq. (16). The near-specular phase function, based on the generalized Van Cittert–Zernike theorem, is given by[1]

$$P_{\text{nspec}}(\theta_r, \theta_i) = N_{\text{nspec}}(\theta_i, C) \exp\left[-\frac{(\sin\theta_r + \sin\theta_i)^2}{(C\cos\theta_i)^2}\right] \cos\theta_r, \tag{19}$$

where C is a constant related to the surface roughness statistics. The diffuse phase function is given by[7]

$$P_{\text{diff}}(\theta_r, \theta_i, m, \alpha) = N_{\text{diff}}(\theta_i, \alpha, m) \frac{[\alpha\cos(\theta_i)]^{m-1}}{[|\sin(\theta_r) + \sin(\theta_i)|]^m + [\alpha\cos(\theta_i)]^m} \cos(\theta_r), \tag{20}$$

where α is the half-angle of the reflected beam, m is an exponent chosen to best fit the data ($m = 2$ for a Lorentz phase function), and N_{diff} is a normalization factor. The Lambertian phase function is given by

$$P_{\text{Lam}}(\theta_r) = \frac{1}{\pi}\cos(\theta_r), \tag{21}$$

where the function is defined on a hemisphere.

The three phase functions defined by Eqs. (19)–(21) are distinctively different in shape, as illustrated by Fig. 3. The wing region away from the specular point falls off much more slowly for the diffuse function as opposed to the near-specular function (Gaussian). This is significant because the Gaussian phase function is commonly applied. However, as the

next section will clearly demonstrate, the diffuse phase function, as defined by Eq. (20), provides a superior fit to experimental data (this is especially true for very rough surfaces with significant bulk scatter, e.g., paints, such as that in this study).

The paper by Duncan et al.[1] gives some theoretical insight into the phase functions applied in this paper. It is shown that for Gaussian surface roughness and for near-specular reflection, the phase function will also be Gaussian. However, if the photon of light is significantly delayed by the surface roughness or by penetrating a dielectric surface and then for backscattered to the observer, the phase function can take a power law form similar to Eq. (20).

To complete the near-specular BRDF model, the following formula for the angle averaged single surface reflection coefficient is defined[7]:

$$R_{\text{ave}}(\theta_i, \alpha, n) = \int_0^{\frac{\pi}{2}} R(\theta, n)\, P_{nS}(\theta, \theta_i; \alpha)\, d\theta, \tag{22}$$

where $R(\theta, n)$ is the Fresnel power reflection coefficient for unpolarized light. To make Eq. (22) computationally efficient, it is approximated by a top-hat function, defined by

$$P_{nS}(\theta, \theta_i) \approx H(\theta, \theta_i) = \left\{ \begin{array}{ll} \left\{ \begin{array}{l} \dfrac{1}{2\alpha} \text{ for } \theta_i + \alpha \le \dfrac{\pi}{2} \text{ and } \theta_i - \alpha \ge 0 \\ \dfrac{1}{\frac{\pi}{2} - \theta_i + \alpha} \text{ for } \theta_i + \alpha \ge \dfrac{\pi}{2} \\ \dfrac{1}{\theta_i + \alpha} \text{ for } \theta_i - \alpha \le 0 \end{array} \right\} & \theta_i + \alpha \ge \theta \ge \theta_i - \alpha \\ 0 & \text{otherwise} \end{array} \right\}, \tag{23}$$

where α is the half-width of the reflected beam.

The TIR for the Lambertian component is described by Kubelka–Munk theory[2] as given by

$$\rho_L(a, \beta_{\text{sca}}) = \frac{\frac{1}{a} - \sqrt{\frac{1}{a^2} - 1} - \left(\frac{1}{a} + \sqrt{\frac{1}{a^2} - 1}\right) \Gamma(a) \exp\left(-2\sqrt{\frac{1}{a^2} - 1}\beta_{\text{sca}} d\right)}{1 - \Gamma(a) \exp\left(-2\sqrt{\frac{1}{a^2} - 1}\beta_{\text{sca}} d\right)}, \tag{24}$$

where a is the albedo, d is the thickness of a film on a substrate with a known TIR,

$$\Gamma(a) = \frac{\rho_{\text{sub}} - \frac{1}{a} + \sqrt{\frac{1}{a^2} - 1}}{\rho_{\text{sub}} - \frac{1}{a} - \sqrt{\frac{1}{a^2} - 1}}, \quad a = \frac{\beta_{\text{sca}}}{\beta_{\text{sca}} + \beta_{\text{abs}}}, \tag{25}$$

where ρ_{sub} is the TIR of the substrate (0 for a freestanding window) consistent with Kubelka–Munk theory and β_{sca} is the scatter coefficient.

To complete the Kubelka–Munk model, a scatter coefficient model for the paint is needed. A typical white paint is composed of a binder mixed with fine, nonabsorbing particles. This produces a scattering medium. Anomalous diffraction theory yields a computationally efficient and robust approximation to Mie theory and a model for the scatter coefficient. The resulting extinction efficiency for a nonabsorbing spherical particle is

$$Q_{\text{ext}}(r') = 2 - \frac{4}{r'} \sin(r') + \frac{4}{r'^2}[1 - \cos(r')], \tag{26}$$

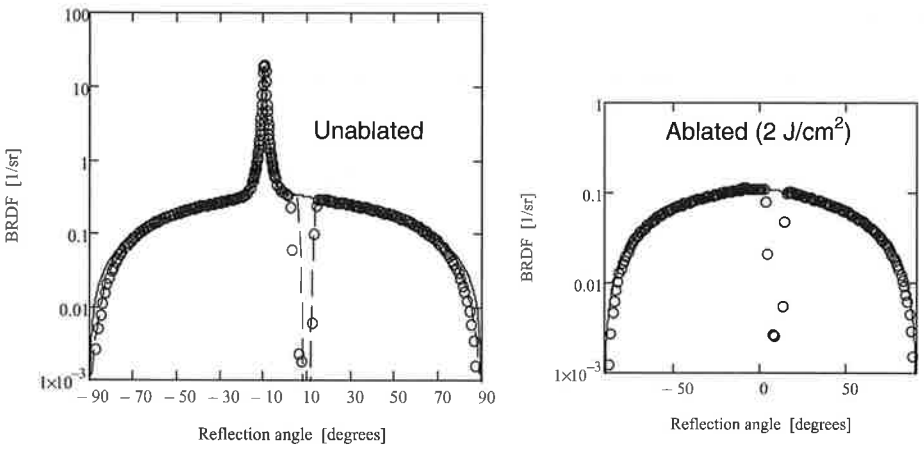

Fig. 4. In-plane BRDF of glossy white paint at 633 nm and an incidence angle of 10 deg.

where $r' = 2(2\pi r_p/\lambda)n_0[(n_1/n_0) - 1]$, r_p is the radius of the spherical particle, n_1 is the refractive index of the particle, and n_0 is the refractive index of the background medium. It is based on plane wave propagation through a spherical particle that is large compared to the wavelength using Huygen's principle.[8] It is also assumed that reflection and refraction can be ignored {that is, $[(n_1/n_0) - 1]$ is small}.[8] Thus the theory emphasizes diffraction and interference effects that often dominate scatter phenomenon.

Based on Eq. (26), the scatter coefficient also can be computed to be

$$\beta_{\text{sca}}(\lambda) = \int_0^\infty \pi r'^2 Q_{\text{ext}}(r', \lambda)\eta(r')\, dr', \tag{27}$$

where η is the size distribution function. Thus, if two transmittance measurements are made with the same particles in different suspension media, the refractive index of the particles can be derived without knowledge of the size distribution function of the particle by taking a ratio of the measured scatter coefficients.

To compute the albedo, an absorption coefficient model for the binder is needed. The model in this case uses an Urbach tail model for the UV absorption edge and an exponential model for IR absorption edge.

4. Results

Figure 4 shows the BRDF for the unablated painted surface and one example of ablated paint for a fluence of $2\,\text{Jcm}^{-2}$. Even though the unablated paint BRDF shows a near-specular peak, it is less than 1% of the TIR. Once the ablation begins, the surface becomes totally diffuse. Therefore, in the following analysis it is assumed that the paint is always diffuse (this will not necessarily be the case for all targets of interest). Thus, the Kubelka–Munk model is used solely for the TIR. The resulting model parameters for the BRDF of the ablated paint for various fluence levels are listed in Tables 1–3 for 633-, 1,064, and 3,390-nm illumination, respectively. The tables also list the measured TIRs for each fluence level. A plot of the TIRs versus the laser fluence is shown in Fig. 5a. A

Table 1. Fitting parameters for paint ablations at 633 nm with $\theta_i = 10$ deg

					Fitting function								
					$AP_{\text{nspec}}(\theta_r, \theta_i, C)$		$AP_{\text{diff}}(\theta_r, \theta_i, m, \alpha)$			$AP_{\text{diff}}(\theta_r, \theta_i, m, \alpha)$			$AP_{\text{Lam}}(\theta_r)$
PRF (Hz)	Pulse energy (μ J)	Raster step (mm)	Fluence (J/cm^2)	TIR	A	C	A	m	α	A	m	α	A
0	NA	NA	0	0.87	0.0025	0.74	0.22	2	38.1	0.38	3	1.8	0.66
18	40	0.15	0.24	0.76	0.0012	0.67	0.13	2	25.5	0.40	3	1.7	0.62
18	50	0.15	0.30	0.65	0.0013	0.74	0.14	2	25.5	0.38	3	1.9	0.51
18	65	0.15	0.38	0.57	8.5e-4	0.67	0.13	2	25.5	0.33	3	1.8	0.44
48	60	0.2	0.71	0.46	—	—	0.17	2	25.5	0.23	3	1.8	0.31
12	600	0.2	1.8	0.32	—	—	0.02	2	25.5	—	—	—	0.30
12	650	0.2	1.9	0.31	—	—	0.035	2	25.5	—	—	—	0.29
24	650	0.2	3.8	0.30	—	—	0.015	2	25.5	—	—	—	0.29
48	650	0.2	7.7	0.35	—	—	0.020	2	25.5	—	—	—	0.33
100	650	0.2	16.0	0.29	—	—	0.017	2	25.5	—	—	—	0.28
500	650	0.2	80.1	0.16	—	—	0.019	2	25.5	—	—	—	0.15
500	650	0.15	106.8	0.20	—	—	0.027	2	25.5	—	—	—	0.19
1,000	650	0.2	160.2	0.16	—	—	0.005	2	25.5	—	—	—	0.16
1,000	650	0.15	213.6	0.09	—	—	0.037	2	25.5	—	—	—	0.07

Table 2. Fitting parameters for paint ablations at 1,064 nm with $\theta_i = 10$ deg

					Fitting function								
					$\rho_{ns} P_{nspec}(\theta_r, \theta_i, C)$		$\rho_d P_{diff}(\theta_r, \theta_i, m, \alpha)$			$\rho_d P_{diff}(\theta_r, \theta_i, m, \alpha)$			$\rho_L P_{Lam}(\theta_r)$
PRF (Hz)	Pulse energy (μJ)	Raster step (mm)	Fluence (J/cm^2)	TIR	ρ_{ns}	C	ρ_d	m	α	ρ_d	m	α	ρ_L
0	NA	NA	0	0.88	7.8e-7	0.63	0.10	2	32.9	0.49	3	1.8	0.75
18	40	0.15	0.24	0.75	3.6e-7	0.62	–	–	–	0.47	3	1.6	0.71
18	50	0.15	0.30	0.63	3.9e-7	0.61	0.09	2	25.5	0.47	3	1.7	0.51
18	65	0.15	0.38	0.54	3.4e-7	0.62	–	–	–	0.31	3	2.4	0.49
48	60	0.2	0.71	0.41	4.1e-7	0.65	0.11	2	25.5	0.30	3	2.1	0.30
12	600	0.2	1.8	0.27	—	—	0.06	2	25.5	—	—	—	0.22
24	650	0.2	1.9	0.29	—	—	0.05	2	25.5	—	—	—	0.26
48	650	0.2	3.8	0.29	—	—	0.04	2	25.5	—	—	—	0.27
100	650	0.2	7.7	0.27	—	—	0.04	2	25.5	—	—	—	0.24
500	650	0.2	16.0	0.11	—	—	0.03	2	25.5	—	—	—	0.09
500	650	0.15	80.1	0.18	—	—	0.04	2	25.5	—	—	—	0.15
1,000	650	0.2	106.8	0.12	—	—	0.02	2	25.5	—	—	—	0.11
1,000	650	0.15	160.2	0.16	—	—	0.19	2	25.5	—	—	—	0.03

Table 3. Fitting parameters for paint ablations at 3,390 nm with $\theta_i = 10$ deg

					Fitting function								
					$\rho_{ns} P_{nspec}(\theta_r, \theta_i, C)$		$\rho_d P_{diff}(\theta_r, \theta_i, m, \alpha)$			$\rho_d P_{diff}(\theta_r, \theta_i, m, \alpha)$			$\rho_L P_{Lam}(\theta_r)$
PRF (Hz)	Pulse energy (μJ)	Raster step (mm)	Fluence (J/cm^2)	TIR	ρ_{ns}	C	ρ_d	m	α	ρ_d	m	α	ρ_L
12	650	0.2	1.9	0.31	1e-3	0.7	0.28	2	30	0.16	3	1.8	0.09
1,000	650	0.2	160.2	0.14	5e-7	0.6	0.07	2	22.3	8e-3	3	4.7	0.09

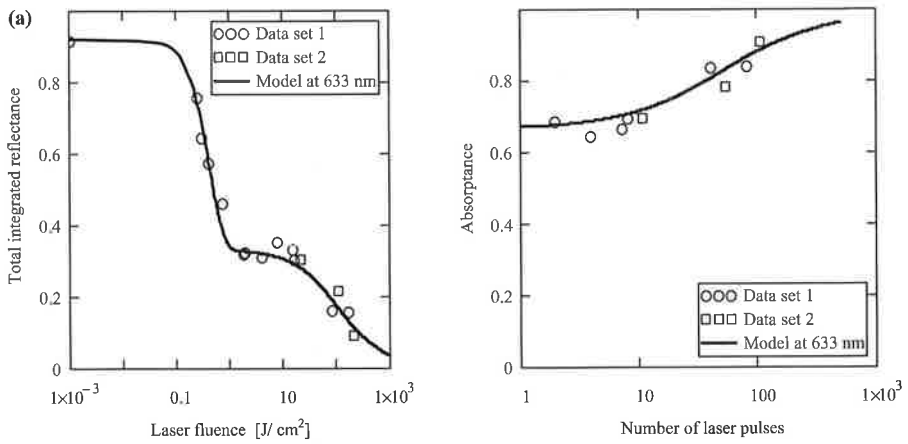

Fig. 5. (a) TIR at 633 nm plotted as a function of laser fluence at 800 nm. The solid curve is based on the Kubelka–Munk model. (b) Surface absorptance as a function of the number of laser pulses with 650 μJ/pulse.

TIR model, based on Kubelka–Munk theory, is also shown. The model assumes a paint thickness of 0.1 cm, a substrate TIR of 0.925, a binder refractive index of 1.49, a paint particle refractive index of 1.85 (e.g., alumina), and a paint particle radius of 2.7 μm with a concentration of $1.3 \times 10^7\,\mathrm{cm}^{-3}$. As the fluence increases, some material is ablated and carbon remains on the surface. The carbon film builds up with increasing fluence, making the surface more absorptive. The following empirical formula for an effective absorption coefficient (per centimeter) of carbon (soot) as a function of laser fluence is used:

$$\beta_{\mathrm{abs,carbon}}(F) = \left[1 - \exp\left(-\frac{F^2}{F_{\mathrm{th}}^2}\right)\right](6.95 + 0.075F), \tag{28}$$

where $F_{\mathrm{th}} = 0.57\,\mathrm{Jcm}^{-2}$ is the ablation threshold fluence. The first factor in the equation represents a threshold function for the generation of carbon and for paint surface damage. The second factor represents the increase in the absorption coefficient caused by the deposition of carbon during laser ablation. The model parameters are determined empirically by fitting to the experimental data. The absorption coefficient model is well below the full density value for carbon because a small nonuniform amount of carbon is generated, which is concentrated on the surface rather than throughout the paint thickness. Figure 5a shows that Eq. (28) is in good agreement with the measured data. Based on this model for the TIR, the absorptance can be obtained by subtracting the TIR from unity. This result is plotted in Fig. 5b as a function of the number of laser pulses that illuminate the entire area of interest.

Equation (27) deserves some explanation. The threshold function contains an Arrhenius-type potential of the general form

$$\exp\left(-\frac{E_v}{E_0}\right),$$

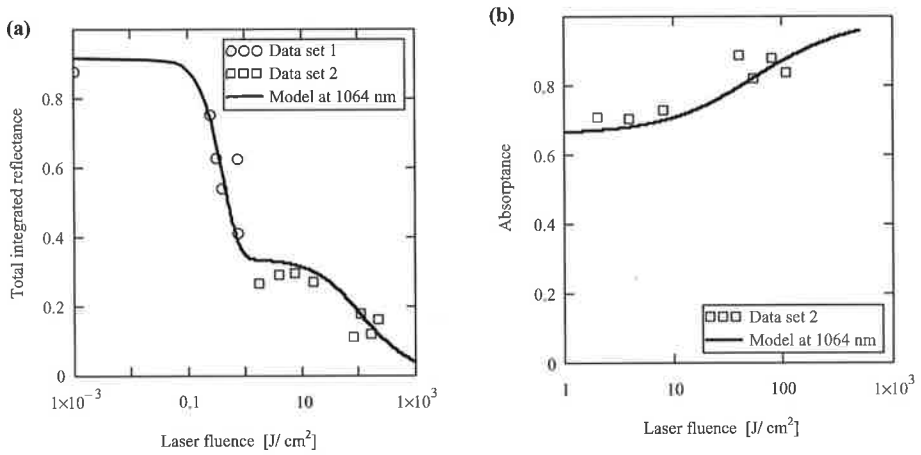

Fig. 6. (a) TIR at 1,064 nm plotted as a function of laser fluence at 800 nm. The solid curve is based on the Kubelka–Munk model. (b) Surface absorptance as a function of the number of laser pulses with 650 μJ/pulse.

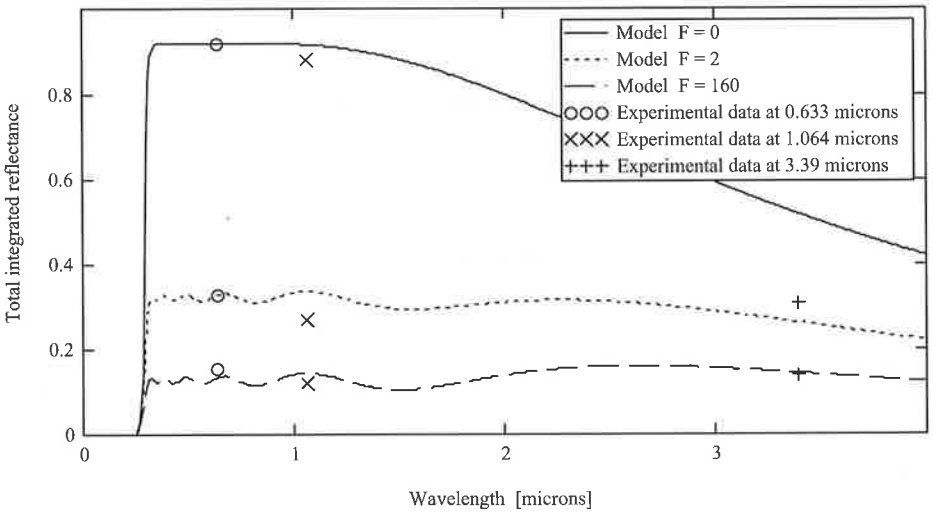

Fig. 7. The TIR of the paint as a function of wavelength for different levels of fluence.

where E_ν is photon energy on the target and E_0 is a damage threshold energy. The photon field energy is

$$E_\nu = M_\nu hf,$$

where M_ν is the number of photons, h is Planck's constant, and f is the photon frequency. Because multiphoton absorption is the typical damage mechanism for dielectric media, we consider a two-photon absorption rate equation, as given by

$$\dot{M}_\nu = \dot{M}_2 \approx \gamma I^2, \tag{29}$$

where γ is a rate factor and I is the intensity in watts per square centimeter. The fluence is intensity times the duration of the radiation. Thus, the photon energy is proportional to the square of the fluence. This explains the form of the threshold function in Eq. (28).

Figure 6 compares the TIR model as a function of wavelength for various ablation levels to experimental data at 633, 1,064, and 3,390 nm. The model predicts the TIR at 800 nm where the ablating laser actually operated. In fact, the entire near-IR region is covered by the model. This is an initial attempt at developing a more complete quantitative engineering model for target absorption characteristics related to the illuminating laser fluence.

5. Conclusions

A relatively simple, semiempirical model is applied to represent the absorbance of an ablated paint as a function of wavelength and laser fluence. The model distinguishes between near-specular and diffuse reflectance. This is important because the TIR is very different for each case. An averaged Fresnel coefficient is used for the near-specular component, and Kubelka–Munk theory is used for the diffuse case. For the paint studied here, the reflectance was essentially diffuse; thus Kubelka–Munk theory is emphasized. The model is intended to provide a quantitative approach to model laser coupling into painted surfaces.

Future work needs to be done on the optical properties of carbon soot generated by laser ablation, the amount of carbon generated for particular binders, and the spatial distribution. This will make the model less empirical and more applicable to other surfaces.

6. Acknowledgments

The authors gratefully acknowledge the support of the Internal Research and Development Committee at the Johns Hopkins University Applied Physics Laboratory.

References

[1]Duncan, D.D., D.V. Hahn, and M.E. Thomas, *Proceedings of SPIE Optical Diagnostic Methods for Inorganic materials IIII* **5192** (2003).

[2]Kubelka, P., and F. Munk, Z. Tech. Physik **12**, 593 (1931).

[3]Ogilvy, J.A., *Theory of Wave Scattering from Random Rough Surfaces*, Institute of Physics Publishing (1991).

[4]Stover, J.C., *Optical Scattering, Measurement and Analysis*, SPIE Optical Engineering Press (1995).

[5]Stuart, B.C., M.D. Feit, S. Herman, A.M. Rubenchik, B.W. Shore, and M.D. Perry, Phys. Rev. B **53**, 1749 (1996).

[6]Thomas, M.E., *Optical Propagation in Linear Media*, Oxford University Press (2006).

[7]Thomas, M.E., D.W. Blodgett, and D.V. Hahn, *Proceedings of SPIE Optical Diagnostic Methods for Inorganic Materials III* **5192**, 158 (2003).

[8]van de Hulst, H.C., *Light Scattering by Small Particles*, Dover (1981).

[9]Zhigilei, L.V., P.B.S. Kodali, and B.J. Garrison, J. Phys. Chem. B **102**, 2845 (1998).